

Alma Mater Studiorum Università di Bologna
Archivio istituzionale della ricerca

Reconstruction of a Reference Subsoil Model for the Seismic Microzonation of Gori (Georgia): A Procedure Based on Principal Component Analysis (PCA)

This is the final peer-reviewed author's accepted manuscript (postprint) of the following publication:

Published Version:

Giallini, S., Paolucci, E., Sirianni, P., Albarello, D., Gaudiosi, I., Polpetta, F., et al. (2021). Reconstruction of a Reference Subsoil Model for the Seismic Microzonation of Gori (Georgia): A Procedure Based on Principal Component Analysis (PCA). BULLETIN OF THE SEISMOLOGICAL SOCIETY OF AMERICA, 111(4), 1921-1939 [10.1785/0120200341].

Availability:

This version is available at: <https://hdl.handle.net/11585/941595> since: 2023-09-13

Published:

DOI: <http://doi.org/10.1785/0120200341>

Terms of use:

Some rights reserved. The terms and conditions for the reuse of this version of the manuscript are specified in the publishing policy. For all terms of use and more information see the publisher's website.

This item was downloaded from IRIS Università di Bologna (<https://cris.unibo.it/>).
When citing, please refer to the published version.

(Article begins on next page)

This is the final peer-reviewed accepted manuscript of:

Silvia Giallini, Enrico Paolucci, Pietro Sirianni, Dario Albarello, Iolanda Gaudiosi, Federica Polpetta, Maurizio Simionato, Francesco Stigliano, Nino Tsereteli, Zurab Gogoladze, Massimiliano Moscatelli; Reconstruction of a Reference Subsoil Model for the Seismic Microzonation of Gori (Georgia): A Procedure Based on Principal Component Analysis (PCA). Bulletin of the Seismological Society of America 2021; 111 (4): 1921–1939.

The final published version is available online at:
<https://doi.org/10.1785/0120200341>

Terms of use:

Some rights reserved. The terms and conditions for the reuse of this version of the manuscript are specified in the publishing policy. For all terms of use and more information see the publisher's website.

This item was downloaded from IRIS Università di Bologna (<https://cris.unibo.it/>)

When citing, please refer to the published version.

**Reconstruction of a reference subsoil model for the seismic microzonation of Gori (Georgia):
a procedure based on Principal Component Analysis (PCA)**

**Giallini S.^{1*}, Paolucci E.², Sirianni P.¹, Albarello D.², Gaudiosi I.¹, Polpetta F.¹, Simionato M.¹,
Stigliano F.¹, Tsereteli N.³, Gogoladze Z.³ and Moscatelli M.¹**

*1 Istituto di Geologia Ambientale e Geoingegneria (IGAG), Consiglio Nazionale delle Ricerche
(CNR), Area della Ricerca di Roma 1, Montelibretti, Italy*

*2 Dipartimento di Scienze Fisiche, della Terra e dell'Ambiente, Università degli Studi di Siena,
Siena, Italy*

3 M. Nodia Institute of Geophysics of I. Javakhishvili Tbilisi State University, Tbilisi, Georgia

**Corresponding author.*

*mailing address: silvia.giallini@igag.cnr.it; enrico.paolucci@unisi.it; pietro.sirianni@igag.cnr.it;
dario.albarello@unisi.it; iolanda.gaudiosi@igag.cnr.it; federica.polpetta@igag.cnr.it;
maurizio.simionato@igag.cnr.it; francesco.stigliano@igag.cnr.it; nino_tsereteli@tsu.ge;
zurab.gogoladze.3@gmail.com; massimiliano.moscatelli@igag.cnr.it*

Declaration of Competing Interests

The authors acknowledge there are no conflicts of interest recorded.

Abstract

This paper focuses on the full exploitation of geological and economically viable geophysical surveys for the seismic characterization of the shallow subsoil in the frame of microzonation studies in urban areas where economic resources for detailed seismic response analyses are scarce. In these conditions, the outcomes of inexpensive geophysical surveys (e.g., based on ambient vibration monitoring or surface wave prospecting) must be fully exploited. To reduce the uncertainties related to these kinds of procedures, their joint interpretation in the light of geological evidence is mandatory. To this purpose, we propose the application of Principal Component Analysis (PCA) to combine the results of distributed single station ambient vibration measurements (HVSr technique) to provide a preliminary zonation of the study area. The zones identified in this way are then characterized by considering the available geognostic boreholes, Vs profiles deduced by the joint inversion of HVSr curves, and available Rayleigh wave dispersion curves deduced from active seismic prospecting (MASW technique). The final outcome allows the definition of a preliminary seismic model of the study area, which is also constrained by the available geological data deduced from on purpose surveys. The proposed approach has been applied to the city of Gori (Georgia). The proposed approach allowed a reliable assessment of buried geometries, geological domains, and the distribution of lithofacies, which can control the local seismic response. In detail, the major role of paleo-valley infills and interfluvial domains has been enlightened by adding in evidence concerning the peculiar stratigraphic relationships and buried morphologies, which may determine 1D and 2D resonance effects.

INTRODUCTION

It is well known that local conditions strongly affect ground motion at vibration periods of engineering interest (Kramer, 1996). Seismic microzonation highlights the geological and geomorphological features which control ground motion by identifying areas characterized by homogeneous seismic behavior at the municipality scale; it represents a tool accepted worldwide for the implementation of seismic mitigation

41 strategies and urban planning management. Since the pioneering work by Medvedev (1965), several attempts
42 have been developed to systematize microzonation studies (e.g., TC4, 1999; DRM, 2004), reflecting national
43 perspectives and seismic rules operating in the respective countries. In Italy, seismic microzonation
44 guidelines were developed in 2008 (WGSM, 2008) and progressively updated because of field experiences
45 (WGSM, 2008; WGSMLA, 2010; Dolce et al., 2011). These Italian guidelines state that seismic
46 microzonation studies can be carried out at three levels of increasing detail, which also involve growing
47 complexity, commitment, and economic efforts (Albarello et al., 2015; Albarello, 2017; Moscatelli et al.,
48 2020). The first level (i.e., Level 1) is a semi-qualitative level and aims to define a reference geological
49 model (from the perspective of forecasting expected seismic effects) for the study area (Amanti et al.,
50 2020a). The subsoil model used at this level focuses on the geometrical characterization of the main
51 geological/geotechnical bodies present in the shallow subsoil, based on pre-existing data and low-cost
52 seismic surveys performed in the study area. As the site response is primarily a function of the mechanical
53 response of the subsoil, reconstructing the characteristics of shallow soil layers is a primary task of a study of
54 the local seismic response. Moreover, the understanding of the spatial distribution of geologic domains is of
55 crucial importance, because their stratigraphy and morphology may determine 1D and 2D resonance effects.
56 The main expected outcome of Level 1 is the “Map of Seismically Homogeneous Microzones” (SHMs map;
57 see Moscatelli et al., 2020) at a 1:5000 or 1:10000 scale. The SHMs map delimitates zones characterized by
58 similar expected co-seismic phenomena by distinguishing i) zones where no ground motion amplification
59 effects are expected (stable zones), ii) zones where amplification is expected due to seismic energy trapping
60 and interference phenomena induced by impedance contrasts in the shallow subsoil or surface morphology,
61 and iii) zones where seismically induced permanent instabilities (such as landslides, liquefaction, surface
62 faulting, densification) may occur. Geological and geotechnical cross-sections of the study area are also
63 provided at this level and possibly traced down to the depths of the local bedrock. Cross sections are of high
64 importance for constraining buried geometries and planning geophysical and geotechnical investigations,
65 supplying quantitative information about possible site effects. These investigations are developed in the
66 framework of Level 2 and Level 3 microzonation studies. Simplified approaches are applied at Level 2
67 (Peruzzi et al., 2016; Paolucci et al., 2020), where 1D seismic resonance phenomena are expected. Level 3
68 microzonation is planned where the complexity of subsoil geometries and rough surface morphology prevent

69 the use of simplified approaches (i.e., Level 2) and where permanent instabilities may occur (Amanti et al.,
70 2020b; Pagliaroli et al., 2019).

71 The primary importance of Level 1 should not be underestimated. Besides being the preparatory (and
72 mandatory) phase for the subsequent levels, its cost-effectiveness also makes it possible to apply it in areas
73 with scarce availability of economic resources. Furthermore, since it provides a first general outlook on the
74 main subsurface features, most critical situations where major efforts must be devoted to highlight possible
75 site effects are outlined at this level of analysis.

76 As stated above, Level 1 studies mainly rely on two pieces of information: i) a re-appraisal of the existing
77 geological/geotechnical data available from previous studies (e.g., geological mapping, geotechnical
78 investigations for building design, boreholes, etc.) and ii) geophysical investigations performed on purpose
79 (Caielli et al., 2020). Single station ambient vibration measurements by Horizontal-to-Vertical Spectral Ratio
80 (HVSr) procedures (Bard, 1998) are largely considered for a preliminary characterization of seismic
81 response during extensive surveys at Level 1 (Molnar et al., 2018). When jointly interpreted with surface
82 wave dispersion curves inferred from active surveys, such as the Multichannel Analysis of Surface Waves
83 (MASW) technique (Park et al., 1999; Foti, 2000; Foti et al., 2011), HVSr values as a function of frequency
84 (HVSr curves) may be useful for constraining the local shear wave velocity (V_s) profile (Albarelo et al.,
85 2011). More interestingly for Level 1 microzonation studies, theoretical investigations (Albarelo and
86 Lunedei, 2010; Lunedei and Malischevsky, 2015) indicate that the shape of HVSr curves reflects the seismic
87 resonance phenomena potentially induced by seismic impedance contrasts, which are of primary importance
88 for the seismic characterization of the subsoil. In particular, it is quite established in the literature that in the
89 presence of a sharp impedance contrast in the subsoil, the HVSr curve shows a marked peak corresponding
90 to the fundamental resonance frequency of the sedimentary cover (e.g., Bonnefoy-Claudet et al., 2006). In
91 view of these observations, it is possible to state that similar HVSr curves indicate the similarity of the local
92 subsoil configuration with respect to the expected local seismic response.

93 To fully exploit the outcomes of ambient vibration measurements, they must be interpreted in the light of a
94 coherent geological/geotechnical model. However, most geophysical measurements only provide 1D point-
95 like information about the subsoil configuration. On the other hand, the geological characterization of the

96 subsoil involves the 2D geometrical assessment of relatively large, buried bodies. To make a comparison
97 possible, the outcomes of HVSR measurements sparsely distributed over the study area must be re-
98 interpreted to identify zones characterized by similar seismic behavior. When many HVSR curves are
99 available (tens of measuring sites are common in seismic microzonation studies), such a comparison cannot
100 be performed manually, and numerical pattern recognition techniques may be of help. The identification of
101 the characteristic patterns limits the amplitude uncertainty often affecting HVSR measurements, by focusing
102 on general features (e.g., the frequency of the peak) less affected by the statistical fluctuations inherent to
103 these kinds of measurements. Moreover, the joint analysis of several HVSR curves may enlighten weak
104 resonance phenomena not clearly visible on single site measurements (e.g., due to the stochastic fluctuations
105 of ambient vibrations), but present at several sites with similar features and representative of actual subsoil
106 configurations. To perform seismic zonation based on the similarity of HVSR data, different approaches have
107 been proposed in the literature. In particular, Bragato et al. (2007) and Ullah et al. (2013) explored
108 procedures based on cluster analysis; Strollo et al. (2012) performed a zonation considering the correlations
109 between HVSR curves and site response functions computed using earthquake data.

110 Among these techniques, Principal Component Analysis (PCA) has been widely used in several fields
111 (Davis, 2002; Wilks, 2006) and recently also proposed for the multivariate analysis of HVSR curves in the
112 context of seismic microzonation studies to identify areas characterized by similar subsoil seismic structures
113 (Paolucci et al., 2017). This approach can be particularly effective as a computational support for evaluating
114 seismostratigraphic heterogeneity over broad areas, and it does not need to consider any prior assumptions.
115 The aim of the present study is applying this procedure to the semi-qualitative (i.e., Level 1) seismic
116 microzonation of the city of Gori, Georgia, and exploring the capabilities of more advanced techniques
117 aiming at better constraining subsoil models for seismic response evaluation.

118 In fact, because the city of Gori is located in a highly seismic area, mainly built on alluvial Quaternary
119 sediments, a study of the subsoil model and of the areas potentially responsible for the local amplification of
120 seismic ground motion could be very important. In the framework of a Georgia-Italy bilateral research
121 project (CNR-SRNSF 2016–2017), a seismic microzonation study of the city of Gori according to the Italian
122 guidelines on seismic microzonation was performed. In this context, an extensive geophysical survey of the

123 study area was carried out using passive HVSR measurements and active surface wave prospecting (i.e.,
124 MASW). The aim of these surveys, supported by the exploitation of existing data (mainly surface
125 geological/geotechnical surveys and shallow borehole logs performed for other purposes), was defining the
126 reference geological model for the seismic microzonation of the urbanized area of Gori. In the following, a
127 short summary of the geological and tectonic settings of the study area is firstly outlined along with the
128 available information about subsoil characteristics and the outcomes of geophysical campaigns. Then, the
129 outcomes of the PCA analysis of HVSR measurements are illustrated and interpreted in the light of existing
130 geological/geotechnical data. Finally, the reference geological model is presented and the geometry of SHM
131 areas are identified and discussed.

132 The results of this study are important because they constitute one of the very first examples of seismic
133 microzonation in Georgia (together with the study just concluded in the city of Mtskheta; Tsereteli et al.,
134 2021). In addition to allowing the Gori territory to be mapped in terms of the expected effects in case of
135 earthquake, the adaptation of the Italian methodology to the Georgian context could be of great use for
136 starting systematic studies of seismic microzonation in Georgia.

137 To better gain an understanding of the procedure followed, in Figure 1 we present a flow chart where each
138 step of the procedure is graphically represented.

139 ***OUTLINES OF THE GEOLOGICAL AND TECTONIC SETTINGS***

140 Seismic risk is a crucial issue for the South Caucasus, due to its position between the still-converging
141 Eurasian and African-Arabian plates (Figure 2a). In detail, the city of Gori is located at the northern margin
142 of the active Achara-Trialeti Fold-and-Thrust belt (ATFT) (Figure 2a) affected by destructive earthquakes in
143 the historical past (Varazanashvili et al., 2006; Varazanashvili et al., 2011).

144 The city of Gori (hereinafter also referred to as Gori) is the administrative center of the Shida Kartli region
145 and is located approximately 90 kilometers north-west of Georgia's capital Tbilisi (Figure 1b). In detail, the
146 study area is within the Kartli Basin, an area of wide basins and valleys enclosed between the Greater
147 Caucasus to the North and the Lesser Caucasus to the South (Figure 1c) and crossed by the Mtkvari River
148 (Furlani et al., 2012).

149 The Kartli Basin is characterized by a foreland sedimentary succession, composed mainly of i) Jurassic,
150 Cretaceous, and Early Cenozoic predominantly shallow water formations and ii) Upper Cenozoic marine and
151 continental sandstones (Figure 2c; Adamia et al., 2010).

152 In the Kartli Basin, Quaternary sediments are almost exclusively of the alluvial type and related to the
153 Mtkvari River system and its tributaries. The sedimentary features and thicknesses of these deposits are
154 related to the Mtkvari River processes. The origin of the Mtkvari River is linked to the transition of the Kartli
155 Basin from a marine to a continental environment (Khain and Malinovsky, 1963). The river plain initially
156 occupied an area located northward of the present one, the depocenter of the Kartli Basin, where the alluvial
157 deposits reach a maximum thickness (up to 200 m; Stinghen, 2011). Later on, Late Pleistocene climate
158 changes coupled with the gradual uplift of the Kvernaqi Range resulted in the total avulsion of the Mtkvari
159 River into its actual course, occupying the area confined between the Kvernaqi Range to the North and the
160 Lesser Caucasus to the South. Near the city of Kareli (19 km west of Gori), it is possible to see how the
161 Mtkvari River abruptly changes its flow, from SW-NE to WNW-ESE (Figure 2c). Moreover, this phase also
162 corresponds to an evolution of the fluvial system from braided (i.e., coarse-grained deposits, with
163 amalgamated multiple, low sinuosity channels; Miall, 1982) to a meandering river, with an increase in
164 channel sinuosity (Furlani et al., 2012).

165 The reconstruction of the Mtkvari River's evolution is fundamental in understanding some of the most
166 important features, which may influence the seismic response (i.e., the paleo-valleys).

167 In detail, Gori is placed at the confluence of the Mtkvari and the Liakhvi rivers. This latter runs through the
168 Kvernaqi Range from North to South and presents a braided course with a rectilinear southeastern direction
169 and, just north of Gori, joins with the Mejuda River, one of its major tributaries. Like the Mtkvari River, the
170 Liakhvi and Medjuda river courses are also likely to have occupied another position in the past. Stinghen
171 (2011) suggests that the Paleo-Liakhvi River passed further west (near the location of Kareli, in Figure 2)
172 and that the uplift of the western sector of the Kvernaqi Range pushed the river to move eastward. In detail,
173 the recent development of anticlines in the western area (just North of the actual Mtkvari plain) played a role
174 in the avulsion of Liakhvi by barring its paleo-river course and leading it to find a more logical course in the
175 pre-existing gorge of the Mejuda River, which probably moved to the East at the same time. However, the

analysis of satellite images suggests that only recently has the confluence of the Mejuda and Liakhvi rivers occupied its present location just north of Gori, probably as an effect of anthropic actions, while previously this confluence was located further north.

Looking at the subsoil of Gori, the city lies on Quaternary alluvial deposits consisting mainly of silty gravels, sands, and subordinately loam deposits, related to both the Liakhvi and Mtkvari rivers. Quaternary deposits in the study area do not reach a significant thickness and cover the geological bedrock, which is made of Tertiary sandstones with terrigenous and carbonate facies (Figure 2c).

For the sake of clarity, it is important to underline that within the text we often refer to the term bedrock, whether in a geological or seismic context. Following the terminology generally used in earthquake engineering, we refer to geological bedrock as a relatively hard, solid rock beneath surface materials such as soil and gravel. If this stiff material is characterized by a shear wave velocity greater than a target value (e.g., 760 m/s, following NEHRP, 2004; 800 m/s according to current Italian and European seismic codes), we differentiate it as engineering bedrock (e.g., Akin et al., 2013). Because they are in the collision zone between the Eurasian and African-Arabian plates (Figure 2a), which are still converging at the rate of 20–30 mm/yr (Reilinger et al., 2006), high seismicity rates characterize the Gori area. In terms of Georgian seismogenic zones (SSZs), the city is located at the northern margin of the Achara-Trialeti Fold-and-Thrust belt (ATFT). Figure 3 shows a schematic representation of the main faults and seismicity, with the locations of both historical and instrumental earthquakes (for details, see Table 1), affecting the study area. The northern tectonic border of the ATFT is represented by the Surami Fault (SF), which is a southward dipping overthrust running ESE-WSW through the territory of Gori (Adamia et al., 2008). Along the Gori segment of the Surami Fault, a destructive earthquake occurred in 1920, with a macroseismic epicentral intensity $I_0 = IX$ (MSK scale) and with an instrumental magnitude $M_w = 6.2$ (Varazanashvili et al., 2006; Varazanashvili et al., 2011). In Gori the effects of this earthquake were documented and correspond to an MSK intensity of VIII–IX: most of the city was heavily damaged and 114 people died (Aivazishvili and Papaplashvili, 1975).

In addition to the Surami Fault, other nearby (within a radius of 25 km from Gori) active fault segments belonging to the ATFT also affect the area: Atskuri Fault (reverse with a left-lateral, strike slip component), Bakuriani Fault (left-lateral, strike slip with a reverse component), and Kaspi Fault (northward dipping

203 overthrust) (AF, BF, and KF, respectively). These faults, if reactivated, could act as a potential source of
204 destructive seismicity for the Gori area.

205 ***DATA GATHERING AND GEOPHYSICAL SURVEY***

206 The seismic microzonation of Gori was carried out starting with the collection and storage of all previously
207 existing data. They consist of a few borehole logs, performed in the eighties for other purposes, and located
208 in the city center (Figure 4). These data are in most cases too shallow (a few meters or less than one meter) to
209 reach the bedrock. These investigations were retrieved through a thorough exploitation of all urban
210 engineering documents stored in the Gori's municipal archive. They were digitized, georeferenced, and
211 finally uploaded into a Geographic Information System.

212 A geophysical campaign was also planned and carried out in order to infer the presence of a seismic
213 impedance contrast in the shallow subsoil, to constrain the shear wave velocity (V_s) characterizing lithotypes
214 present in the study area and map the thickness of Quaternary cover. Forty single station ambient vibration
215 measurements (HVSr) and six MASW surveys were performed (Figure 4). Due to a lack of space, it was not
216 possible to perform 2D array measurements.

217 The geophysical survey covered an area of around 6 km². The single station geophysical survey was
218 performed using digital tromographs (Tromino®), produced by Moho srl, which are compact velocimeters
219 with three orthogonal components. The sampling frequency was set at 128 Hz and the recording length at 40
220 min. Ambient vibration measurements were deployed to try to homogeneously cover the whole urban area of
221 Gori. However, as the locations were carefully selected to avoid the influence of buildings, industrial
222 facilities, and traffic as much as possible, some areas present a lesser concentration of measurements than
223 others.

224 HVSr measurements were analyzed by using Geopsy software (www.geopsy.org). The spectra of the single
225 components were computed by averaging 50-s-long time non-overlapping windows. A baseline correction
226 and a 5% cosine taper were applied to each window, and the spectra were smoothed by using the Konno and
227 Ohmachi (1998) algorithm (with $b = 40$); the windows exhibiting large amplitude transients were excluded

manually. The geometrical mean of horizontal components was used to compute the HVSR values. The quality of the resulting HVSR curve was evaluated following the criteria described by Albarello et al. (2011).

Active MASW surveys were particularly focused on strategic buildings and places, such as the Gori Fortress, Parks of Gori, Museum of Stalin, Gori University, and Rugby stadium (respectively, MW1, MW2-MW3, MW4, MW5, and MW6 in Figure 4), with the aim of providing some useful information for seismic risk prevention. MASW tests were performed by means of a 24-channel digital seismograph equipped with 4.5 Hz geophones with a minimum of 2 m and a maximum of 5 m inter-geophonic spacing. A sampling frequency of 1000 Hz and a total recording length of 1.0 s was applied. The source-to-nearest-receiver offset was adapted to 5 m, while seismic energy was generated using an 8-kg sledgehammer.

Six different Vs profiles (Table 2) were retrieved by considering Rayleigh wave phase velocity dispersion curves obtained by MASW and HVSR curves in a joint inversion approach. In particular, this procedure was performed by using HV-Inv software (<https://w3.ual.es/GruposInv/hv-inv/>). The forward modeling of this algorithm is based on the diffuse field assumption (Sánchez-Sesma et al., 2011) and the inversion procedure takes advantage of local (Simplex Downhill and Interior Point) and global (Montecarlo and Simulated Annealing) search algorithms to support the joint inversion of HVSR and dispersion curves (García-Jerez et al., 2013, 2016; Piña-Flores et al., 2017). In detail, the joint inversion procedure was performed by adopting a two-step inversion scheme (e.g., Picozzi and Albarello, 2007), combining both the global and local search methods mentioned above. The obtained velocity profiles show surface shear wave velocities (Vs) ranging from 200 m/s to 2000 m/s. It should be noted that it was not possible to perform the joint inversion of MW5 due to the lack of closely located HVSR.

248 ***PRINCIPAL COMPONENT ANALYSIS OF THE HVSR DATA***

249 ***METHODOLOGY***

To accomplish PCA, HVSR curves are stored in a $(S \times F)$ matrix $[O]$: F represents the number of frequencies for which the spectral ratios are computed, and S represents the sites where the measurements were carried out. In view of this, the s -th row of $[O]$ (hereafter indicated as $\{O\}_s$) represents the HVSR curve determined at the s -th site. Once the “centered matrix” $[O']$ (subtracting from each element the average value

254 of the corresponding line) is computed, the next step is the estimate of the $(S \times S)$ variance/covariance matrix
 255 $[V_O]$. Following the Spectral Decomposition Theorem (e.g., Wilks, 2006), this matrix is diagonalized
 256 considering the orthogonal matrix $[E]$ and the diagonal matrix $[\Lambda]$, consisting of the S eigenvectors and the
 257 eigenvalues of $[V_O]$, respectively. The eigenvalues, represented by the non-zero elements of $[\Lambda]$, are arranged
 258 in a way such that $\Lambda_{jj} \geq \Lambda_{(j+1)(j+1)}$. An important role is assumed by the trace $tr[\Lambda]$ of $[\Lambda]$, which
 259 represents the overall variance of the HVSR values: therefore, by dividing each eigenvalue by $tr[\Lambda]$, it is
 260 possible to estimate the fraction R_j of variance associated with each j -th eigenvector.

261 Introducing a new $(S \times F)$ matrix $[U]$ (Paolucci et al., 2017), the centered HVSR curve at the s -th site (the
 262 row $\{O'\}_s$) can be seen as a linear combination of S “patterns” defined by the S mutually uncorrelated rows
 263 $\{U\}_j$ of $[U]$:

264

$$265 \quad \{O'\}_s = \sum_{j=1}^S E_{sj} \{U\}_j, \quad (1)$$

266

267 where the E_{sj} are the elements of the matrix $[E]$ (i.e., the “loadings” in the PCA jargon). These patterns
 268 represent the Principal Components (PCs) and identify a set of “characteristic” HVSR trends, each
 269 representative of a fraction of the overall variability of the original dataset. Reversing Eq. 1 in this form,

270

$$271 \quad U_{jf} = \sum_{k=1}^S E_{jk}^T O'_{kf}, \quad (2)$$

272

273 it is possible to point out that the amplitude of the j -th PC at the f -th frequency is proportional to the
 274 amplitude of the HVSR curves measured at the same frequency at all the S sites “weighted” by the E_{jk}^T
 275 coefficients. Substantially, the higher the HVSR value measured at the f -th frequency, the higher the
 276 amplitude of $\{U\}_j$ at the same frequency. Plotting the $\{U\}_j$ (i.e., the “scores” in the PCA jargon) as a
 277 function of the frequency index f , we obtain a pattern that resembles an experimental HVSR curve, but no

quantitative correspondence is expected to exist between respective amplitudes (Paolucci et al., 2017). In particular, the amplitude variation D_j relative to the j -th PC will be defined as

280

$$D_j = \max\{U\}_j - \min\{U\}_j. \quad (3)$$

Moreover, it is worth noting that the sign of the coefficient E_{sj} allows us to identify two “polarities” for each PC. In particular, two opposite patterns are determined, where the maxima and minima of $\{U\}_j$ reverse when the sign of E_{sj} changes: therefore, each PC could represent two different subsoil configurations, characterized by different resonant frequency values. These two “characteristic” patterns will be hereafter indicated as $\{U^+\}_j$ and $\{U^-\}_j$.

An important outcome of the procedure is the parameter R_1 , i.e., the fraction of the overall variance explained by the first and most important PC. Since $R_1 > R_2 > R_3$ and so on, this parameter plays a fundamental role in evaluating the level of heterogeneity of the HVSR measurements and, consequently, of the geological setting responsible for the observed patterns. In particular, high values of R_1 (e.g., 0.8–0.9) indicate a geological configuration (from the seismic behavior point of view) that is relatively homogeneous, where the first PC dominates the others; on the other hand, low values (e.g., 0.3–0.4) can be interpreted as the effect of significant geological heterogeneities in the study area.

Finally, in order to express the relative importance of the j -th PC at the s -th site (and therefore to evaluate which “characteristic” pattern each HVSR curve most closely resembles), a “weight” W_{sj} is introduced as

296

$$W_{sj} = D_j |E_{sj}|. \quad (4)$$

298

This parameter, associated with each PC, allows us to classify the S sites (and therefore the S experimental HVSR curves) as a function on the “dominant” PC among the ones estimated at the s -th site. In particular, the dominant PC at the s -th site (hereafter indicated as $\{\widehat{U}\}_s$) will be chosen as the one corresponding to the

302 maximum \widehat{W}_s among the W_{sj} values relative to the s -th site. It follows that this classification is based on an
303 automatic and objective procedure, and no a priori choice is imposed to select the total number of dominant
304 PCs. This number is related to the heterogeneity level of the HVSR dataset: in general, the lower the value of
305 the R_1 parameter, the greater the number of dominant PCs. For a more complete theoretical treatment of the
306 method, see Paolucci et al. (2017).

307 **RESULTS**

308 PCA was applied to the collected HVSR curves in the range 0.5–10 Hz. The value of the parameter R_1 (0.45)
309 indicates that the most important PC explains about 45% of the overall variance: this suggests a rather
310 heterogeneous subsoil configuration. The shape of the PCs dominating at least one site is shown in Figure 5.
311 The first PC includes two patterns, PC+1 and PC-1: the first one, characterized by a clear maximum at 5.5
312 Hz, is the most representative of the study area, considering that it dominates 15 sites out of the 40
313 considered. The second and the third PCs, both explaining about the 20% of the overall variance, also
314 include two patterns each (PC+2 and PC-2; PC+3 and PC-3). Of particular importance is the PC-2 pattern,
315 which dominates 8 out of 40 sites and is characterized by a peak at about 4 Hz. The remaining two dominant
316 PCs (which explain together about 10% of the overall variance) present one pattern each (PC-4 and PC-5)
317 that shows a maximum at frequencies close to 1 Hz.

318 Figure 6 shows the spatial distribution of the identified dominant patterns in relation to the location of the
319 single-station HVSR measurements. As one can see, the PCs (mainly the two most important ones, i.e.,
320 PC+1 and PC-2) tend to clusterize by identifying rather well-defined zones. Considering also the narrow
321 areas characterized by an evident heterogeneity, it is possible to outline a preliminary zonation (dashed black
322 lines in Figure 6), where a homogeneous seismic response is expected within each zone. To verify this
323 hypothesis, the experimental HVSR curves included in each zone are plotted together and shown in the insets
324 of Figure 6. It is possible to note the good similarity among the experimental curves within each zone.
325 Computing the average HVSR curve within each zone provides evidence of a representative trend by
326 highlighting the specific resonant frequencies for each detected zone. Observing the frequency of the main
327 peak, it is possible to note a progressive decrease of this value moving from south (10 Hz; Zone 7) to north
328 (3.5 Hz; Zone 4). Considering the approximate relationship proposed by Albarello et al. (2011), this feature

329 highlights the presence of a main resonant interface that deepens northward, passing from 5–10 m to 20–30
330 m depth. Still moving northward, Zone 3, which shows a main peak at 5.5 Hz, denotes a slight rise of the
331 interface, while the other two zones (Zones 1 and 2) present patterns characterized by a main peak at about 1
332 and 1.5 Hz. This peak, related to a deeper impedance contrast (of the order of 200 m depth), is also barely
333 visible in the zones located in the central part of the study area (Zones 3, 4, and 5): this feature suggests that
334 such an interface, although not very significant in terms of seismic response, is present in almost the entire
335 investigated area.

336 ***REFERENCE GEOLOGICAL MODEL (FROM THE SEISMOLOGICAL PERSPECTIVE)***

337 ***DEFINITION OF THE ENGINEERING GEOLOGICAL MAP (EG_MAP)***

338 A robust understanding of the subsoil architecture is an indispensable element for the construction of a
339 reference subsoil model from the perspective of its seismological use and, in particular, in the identification
340 of the SHMs. However, the reconstruction of the SHMs requires an intermediate process of transition from a
341 purely geological-geomorphological to an engineering-geological map (EG_map) (with related cross
342 sections). In the EG_map, we partially lose the chronostratigraphic connotation of the individual geological
343 units and point out their geotechnical features.

344 We performed a preliminary field geological survey in the study area to try to recognize the outcropping
345 lithotypes. Regarding instead the reconstruction of the spatial depth variation of the erosional surface
346 shaping, it has greatly benefited from the PCA of the HVSR curves.

347 We developed the reference subsoil model of the study area from the perspective of its seismological use.
348 This was possible thanks to the integration of results obtained by PCA with the geological survey
349 observations, geognostic data available from previous studies (borehole logs), and newer geophysical
350 investigations acquired specifically for this work (HVSR and MASW).

351 Firstly, we mapped outcropping geological bodies and identified the lithostratigraphic units (gg_units)
352 characterizing the geological subsoil model of the study area and their bedding. The complex
353 geological/tectonic context has strongly influenced the geomorphological evolution of the studied area,
354 resulting in reliefs at about 650 m a.s.l., made mainly of Oligocene and also to a minor extent Eocene

deposits, usually outcropping strongly fractured and weathered. These materials belong to the geologic substratum: in particular, Oligocene terrigenous/shallow marine deposits mainly consist of arenaceous to pelitic sandstones with inclusions of conglomerates, while Eocene deposits are made of an alternation of lithotypes (arenites and pelites) of turbiditic units.

Regarding the Quaternary cover, we firstly differentiated between Holocene covers (which the city lies on) and Pleistocene terraces, occurring about 40 meters on the top of the relief in the eastern part of Gori. Then, the interpretation of the available borehole logs allowed us to differentiate them based on lithological features.

Following Bramerini et al. (2018), we derived the EG_map and relative cross sections (Figure 7a–c) by converting the lithostratigraphic units (gg_units) into engineering-geological units (eg_units) and assigning them to distinct categories: “covering terrains” units or “geological bedrock” units, depending on (i) age, (ii) features, (iii) stratigraphy position, and (iv) depositional environment. Table 3 summarizes the correlation among geological units (gg_units), the lithological description of identified geological lithosomes (i.e., geological bodies with a distinctive three-dimensional geometry that may be mutually intertongued with one or more adjacent bodies; Wheeler and Mallory, 1956), the depositional ambient, and, finally, the assigned engineering-geological code (eg_units).

The lithologies of covering terrains were classified via the *ASTM Unified Soil Classification System* (2017), consisting of two capital letters referring to the dominant lithology and additional information, such as the grain size, degree of cementation, and water content. In addition, the covering terrains code presents two more lowercase letters, referring to the depositional ambient (see Table 3). Regarding the classification of the geological bedrock, it was identified by 2- to 4-letter acronyms based on the i) lithology (massive, cemented granular, overconsolidated cohesive, lithotype alternation, etc.), ii) stratification, if it exists (i.e., stratified, non-stratified), and iii) degree of fracturing or weathering.

Borehole log data analysis helped us to determine that covering terrains in Gori consist of alluvial deposits (identified with the code “es”), mainly made of gravels and sandy gravels, with up to 2-m-thick clayey lenses (GM in Figure 7). Sporadically, the thickness of these clayey lenses exceeds 3 m (CL in Figure 7). Moreover, in the southern sector of the city, the borehole stratigraphies (i.e., borehole logs n. 8, 2, 16, and 14

382 in Figure 7) indicate the presence of a sandy lithosome about 15 m thick (SW in Figure 7). Finally,
383 Pleistocene terrace deposits are represented by the GW-tf code (see Table 3), being made primarily of
384 conglomerate and gravel deposits.

385 The identification of these lithosomes is an essential issue, as they can affect seismic waves propagating
386 from the bedrock to the surface due to their peculiar dynamic characteristics (i.e., shear modulus and
387 damping ratio), mainly depending on the nature of the soil. It is well known that the initial stiffness is a
388 fundamental soil property relevant to the prediction of the amplification effects of earthquakes and,
389 therefore, a required input for seismic response analysis is the small-strain shear modulus for each layer
390 (Crespellani and Simoni, 2007). It follows that the representation of different lithosomes in the Engineering
391 Geological map is of crucial important in a seismic microzonation study. It drives, indeed, the selection of
392 the correct curves describing the modification of the initial stiffness and damping versus strain (selected on
393 the basis of relations found in the published literature or discovered after specific laboratory tests) in non-
394 linear models.

395 Regarding the geological bedrock, in Gori the terrigenous/shallow-marine sandstones and conglomerates
396 which were Oligocene in age were classified as “cemented, granular layered lithotypes” (GRS) (Figure 7).
397 Additionally, Eocene turbiditic deposits were classified as “alternation of lithotypes, layered” (ALS). These
398 geotechnical units largely crop out in the study area, presenting a high level of weathering and fracturing
399 (SFGRS and SFALS, respectively, in Figure 7). The evaluation and representation on the map of the jointing
400 degree of the bedrock units are necessary due the fact that it may result in a lower V_s of the rock mass.
401 Consequently, they make bedrock units potentially responsible, as well as the overlying covers, for the
402 modification of the ground motion.

403 To better constrain the two cross sections, PCA Zonation resulting from the cited methodology is added to
404 the map (Figure 7a). The spatial distribution of each PCA zone was reported along the cross sections (Figure
405 7b, c).

406 As main result of the PCA, we found that in the study area, HVSR shows two main peaks, respectively, in
407 high (3.5–10 Hz) and low (1–1.5 Hz) frequency ranges.

408 In detail, with the exclusion of Zone 1, where the high frequency peak is probably related to the presence of
409 an upper weathered/jointed portion of GRS (SFGRS), we interpreted the spatial variability of the higher
410 frequency peak as the heterogeneity of the buried morphology of the covering terrain/GRS contact. This
411 layer represents the first resonant interface. Interpreting in a geological/geotechnical key the shear wave
412 velocity profiles obtained by the joint inversions of the Rayleigh wave velocity dispersion and HVSR curves
413 (Table 2), we assume that the covering terrains reach up to a maximum of 600 m/s, whereas GRS bedrock
414 shows Vs ranging from 750 m/s to 1200 m/s. In particular, we assigned an averaged Vs of 500 m/s to the
415 recent alluvial deposits (comprising GM-es, SW-es, CL-es), an averaged Vs of 600 m/s to the old fluvial
416 terraces (GW-ft), and an averaged Vs of 1000 m/s to the GRS bedrock. Taking into consideration this
417 information, we were able to constrain the thickness of the identified eg_unit and, therefore, the depth of the
418 first resonant interface (Figure 7).

419 The cross sections in Figure 7b, c show the covering terrain, lying upon the erosional surface shaping the
420 GRS bedrock, with a lateral varying thickness ranging from 5 to 35 m, where the lower thickness
421 characterizes the northern sector of the study area (Zone 2 in Figure 7a). However, in the frequency range
422 investigated by PCA (0.5–10 Hz), Zone 2 presents only the lower frequency peak (1.5 Hz). Consulting the
423 available borehole data, we assumed that, in this Zone, covering terrains present a thickness ranging between
424 5–8 m, as testified by borehole n.15 (location reported in Figure 7a), which reaches the GRS bedrock at 5.5
425 m depth. This means that, in this portion of the study area, the higher resonance frequency is likely to be
426 found in a frequency range higher than that investigated by PCA and at about 16–25 Hz. Finally, the
427 maximum covering terrain thickness was individuated within Zone 4, where HVSR measurements highlight
428 a higher frequency averaged peak of 3.5 Hz. Here the GRS bedrock interface depth was estimated at about
429 35 m. Regarding the lower frequency peak revealed by each PCA Zone, with the exclusion of Zone 6 and
430 Zone 7, considering the geological context and geological field survey, we linked it to the GRS/ALS
431 boundary, reaching its maximum depth (> 250 m) in the southern sector of the study area and precisely
432 within Zone 6 and Zone 7 (Figure 7a). In these sectors, the GRS/ALS interface is likely to be too deep to be
433 detected at frequencies ≥ 0.5 Hz.

434 The linear features of the buried morphology, derived from the interpretation of our results, are reported in
435 Figure 7.

436 Summarizing our results, the stratigraphic architecture of the Gori subsoil shows, in the corresponding PCA
437 Zone 4, a stack of paleo-valley infills that is up to 35–40 m deep and 0.5 km wide, mainly composed of
438 gravels and sandy gravel deposits (Figure 7). This buried paleo-valley, running from NE to SW, is bounded
439 by two buried interfluvies (i.e., a region of higher land on the edge of a river valley and/or between two
440 connected river valleys) (PCA Zones 3 and 5) where the Oligocene bedrock is found at lower depths (~11–
441 22 m). Finally, moving north and south (PCA Zones 2 and 6), we find two areas where the bedrock is almost
442 outcropping and the Holocene alluvial cover is just a few meters thick (< 10 m). Our results suggest that a
443 paleo Liakhvi River likely passed to the east of the hill currently arising at the center of Gori (where the
444 Fortress of Gori sits), oriented NE to SE. It probably ran along the western edge of the relief bounding the
445 eastern part of the city and where Pleistocene terraced deposits are currently preserved. In the northern sector
446 of the study area, despite the fact that we expected another zone of fluvial incision operated by the Mejuda
447 River, we found, on the contrary, an area of lower Holocene thickness cover (< 10 m). This result is
448 supported by the previously mentioned hypothesis that, in the recent past, the confluence of the Mejuda and
449 Liakhvi rivers was further north. In light of this hypothesis, only the Liakhvi River processes would have
450 acted on the buried bedrock morphology in the Gori area.

451 ***DEFINITION OF THE SEISMICALLY HOMOGENEOUS MICROZONES (SHMs)***

452 The engineering-geological reconstructions presented earlier (Figure 7), integrated with the geological
453 interpretation of PCA zonation, drove us in the detection of nine homogeneous domains, or microzones
454 (Figure 8). The microzones have been defined by overlaying the thickness of the covering terrains
455 characterizing the identified geological domains on the EG_map, resulting in a map of SHMs (Figure 8a).
456 Following the Italian guidelines for seismic microzonation (WGMS, 2008), stable zones (i.e., zones
457 constituted by outcropping seismic bedrock with flat topography) are absent in the Gori, as the engineering
458 bedrock ($V_s \geq 800$ m/s) is always covered by a relatively thick package of covers or presents a high
459 fracturing/weathering degree.

460 Stable zones prone to ground amplification widely prevail all over the Gori area, with the recognition of only
461 one instable zone.

462 The type-stratigraphy of each microzone is synthesized by logs in Figure 8b, reporting the stack of the
463 EG_map units.

464 ***Stable zones prone to ground motion amplification***

465 Microzone 1: This microzone corresponds to the Gori hill and relief slopes inside the Gori area, where GRS
466 bedrock underlies a thin (15–20 m) fractured/weathered layer.

467 In this microzone, noise measurements (location also reported in Figure 8) show an HVSR peak amplitude <
468 2 at 6–7 Hz, related to the low impedance contrast between weathered/fractured and intact geological
469 bedrock. In this microzone we do not expect a significant amplification of ground motion linked to
470 stratigraphy effects. Considering both the Gori hill shape ($H/L \sim 0.35$, H being the maximum height of the
471 ridge and L being the half-width at the base; e.g., Paolucci, 2002) and an estimated slope degree $> 15^\circ$ for the
472 relief in the eastern part of the city, we do not exclude the possibility of 2D topographic effects. However,
473 HVSR measurements do not highlight the presence of preferential polarized peaks (e.g., Pagliaroli et al.,
474 2019). In this case, numerical 2D modeling will be necessary for a reliable seismic response evaluation.

475 Microzone 2: This microzone contains the alternation of sandstone and marls layers cropping out with a high
476 fracturing/weathering degree, in the south part of Gori and referring to Eocene turbiditic deposits. No HVSR
477 measurements were performed in this part of the city and we have no information about the thickness of the
478 upper fractured/weathered portion derived during this study.

479 Microzone 3: This microzone corresponds to the paleo-valley of the Liakhvi River, infilled with up to 35–40
480 m of alluvial, mainly gravel and sandy gravel, deposits. In this zone the superimposition of the relatively soft
481 alluvial sediments on top of the Oligocene bedrock represents a predisposing factor for ground motion
482 amplification. The shape ratio (h/D , where h is the thickness of the soil deposit and D is the half width of the
483 valley; Bard and Bouchon, 1980) of this paleo-valley, considering that its upper portion is not laterally
484 confined, is always < 0.25 (corresponding to that of a valley where 2D resonance effects start to occur; Bard
485 and Bouchon, 1985). We expect that the 1D site response would account for most of the site effects at the

486 paleo-valley centre. 2D phenomena may be expected at valley edges (the “basin edge effect” in the sense of
487 Anderson, 2007). To provide a quantification of basin edge effects useful from an engineering viewpoint and
488 to better understand the phenomena controlling seismic response, numerical modeling (1D and 2D) will be
489 necessary.

490 Microzone 4: This microzone consists of buried interfluves, partially incised in the northern part of the study
491 area by the minor Mejuda River stream, which flows into the Liakhvi River to the West, with up to 20 m of
492 alluvial deposits (gravels, sandy gravels with loamy layers), probably also related to the Liakhvi River. As in
493 Microzone 3, we expect ground motion amplification linked to stratigraphic effects related to the recent
494 alluvial cover lying on the Oligocene bedrock.

495 Microzones 5, 6, 7: Within the interfluve domains, sandy (Microzones 5 and 6) to clayey (Microzone 7)
496 lithosomes up to 15 m rest directly on the bedrock (Microzone 5) or present a gravel/sandy gravel interlayer
497 (Microzones 6 and 7). The subsoil stratigraphy of these microzones is likely to cause an amplification of
498 seismic waves related to the stratigraphic effects, higher than in the previously mentioned microzones, due to
499 a probably higher impedance contrast between a softer deposit (due to a higher presence of clays and sands
500 than in other parts of the study area) and the Oligocene bedrock. This assumption seems to be justified also
501 by the amplitude of the only HVSr measurement performed in these microzones (HVSr n.37 in Figure 8a),
502 which shows an amplitude level of 2.6 (associated with the shallow resonance interface), higher than those
503 exhibited by HVSr measurements performed in previous microzones.

504 Microzone 8: This microzone contains an area of thin recent alluvial deposits (< 10 m) of the
505 Liakhvi/Mejuda River (north side) and Mtkvari River (south side), made of gravel and sandy gravel resting
506 on bedrock. In this microzone HVSr measurements present a higher value of the peak amplitude (min. value
507 = 2.6; max. value = 4.1) but at frequencies > 17 Hz (within a frequency range of 17–30 Hz), which is about
508 the upper limit of the engineering interest frequency range (0.5–20 Hz; Albarello and Lunedei, 2010).

509 Microzone 9: This microzone consists of Pleistocene terraced deposits, up to 35 m thick, consisting of gravel
510 and conglomerate deposits, resting on seismic bedrock.

511 ***Unstable zones prone to permanent ground deformations***

512 These zones typically include small areas susceptible to landslides. In detail, in Figure 8 we identify one
513 zone prone to instability on the Gori Hill, represented by an undefined landslide detected during the
514 geological field survey.

515 ***DISCUSSION AND CONCLUSIONS***

516 The paper presented here has addressed an application of the PCA of HVSR to the preliminary seismic
517 microzonation of Gori (Georgia). The choice of this case study comes from the need to provide a first
518 outcome toward reducing the seismic risk of Gori, supplying local administrations with a knowledge base of
519 local seismic hazards that is useful for effective seismic risk mitigation strategies.

520 The PCA let us obtain a spatial distribution of the identified HVSR dominant patterns (which represent the
521 Principal Components) and to derive the zones characterized by similar seismic behavior, also allowing us to
522 measure the level of seismo-stratigraphical heterogeneity in the explored area.

523 The interpretation of the results of the PCA of HVSR, in light of the geological and tectonic framework,
524 integrated with data coming from different sources, both geological/geognostic (outcrops, boreholes) and
525 geophysical (MASW), let us achieve an effective reduction of the uncertainty linked to the reference
526 geological model.

527 The approach considered here permitted us to do the following: (1) deduce the buried geology domains and
528 retrieve the stratigraphic architecture of the Gori area; and (2) obtain 3 maps at 1:10,000 scale representing
529 the local condition of the study area, highlighting the geological and geotechnical features (geological map
530 and geotechnical map, respectively) and the spatial distribution of zones characterized by an expected
531 homogeneous seismic response (map of Seismically Homogeneous Microzones). In detail, the geological (in
532 terms of stratigraphic architecture reconstruction), geotechnical (in terms of lithosome detection and their
533 representation with specific geotechnical codes), and geophysical (in terms of representative resonance
534 frequencies attributed to specific geological domains and the shear wave velocity of each detected lithotype)
535 techniques helped us (1) to recognize the presence of a paleo-valley and paleo-interfluvies, likely to be
536 associated with a paleo-course of the Liakhvi River and (2) to infer how these buried domains could control
537 the local seismic response.

538 The maximum expected ground motion amplifications correspond with the buried interfluvies covered by
539 recent alluvial deposits, in particular, where the superimposition of soft sediment (sands) on the stiff rock
540 consisting of the Oligocene bedrock (Microzone 5) is observed. Other non-negligible amplification
541 phenomena, related to both the stiffness contrast and buried morphology, are expected for the paleo-valley
542 infill (Microzone 3). However, due to the expected better mechanical properties of the infill and the low
543 shape ratio of the reconstructed buried geometry, it is inferred that the relevance of these phenomena is lower
544 with respect to areas where the bedrock is overlaid by younger and softer deposits. However, we do not
545 exclude for this microzone the influence of edge effects.

546 In summary, these results helped to highlight areas where 1D and 2D numerical simulations, when
547 performing MS studies in the Gori area, will help in the evaluation of the site effects governing the local
548 response.

549 This study addresses the issue of proposing a new integrated methodology, whose effectiveness and
550 reliability can be very useful when a large amount of geophysical data are available and/or HVSr curves
551 have to be grouped to provide insights for reference subsoil models. Unlike other approaches (e.g., cluster
552 analysis), this is possible without any “ex-ante” assumption about the number and localization of explored
553 patterns. Moreover, this procedure is significantly faster from a computational point of view: it allows the
554 management and analysis of hundreds of measurements within a few seconds on a common personal
555 computer. Concerning the shortcomings, this methodology does not allow us to perform a completely
556 automatic zonation just by grouping the locations of the measurements characterized by the same dominant
557 PC: as shown in Figure 5, in some cases different PCs can highlight slight differences among the
558 experimental curves, especially if a large number of dominant patterns (e.g., higher than three) is involved.
559 In view of this, to better evaluate the overall data heterogeneity, it is recommended to check if curves
560 belonging to two or more dominant PCs can be grouped together. In this respect, the proposed approach can
561 be considered a computer-aided grouping procedure.

562 **DATA AND RESOURCES**

- 563
- 564 • *Borehole data used in this study were kindly provided by the Gori City Hall.*
 - 565 • *Geophysics measurements used in this work were collected as part of a Georgia-Italy bilateral research project (CNR-SRNSF 2016-2017).*

- The single station geophysical survey was performed using digital tromographs (Tromino®) (<http://www.tromino.it>).
- HVSR measurements were analyzed by using Geopsy software (www.geopsy.org).
- All cartography products were made using QGIS software, an open-source Geographic Information System (GIS) (<https://qgis.org/en/site/about/index.html>).
- For information on historical earthquakes, we consulted the Earthquake Catalogue of Georgia (2018). Tbilisi, Georgia, Nodia Institute of Geophysics (<http://www.ig-geophysics.ge/sector1-eng.html>).
- All other data used in this paper came from published sources listed in the references.

Acknowledgements This work has been carried out within the framework of the CNR/SRNSF joint research project “Preliminary study for the assessment of seismic risk in strategic cities of Georgia” (project leaders N. Tsereteli for Georgia and M. Moscatelli for Italy; <https://www.cnr.it/en/bilateral-agreements/project/2193/preliminary-study-for-the-assessment-of-seismic-risk-in-strategic-cities-of-georgia>), and the NATO project S/P G4934 “Georgia Hydropower Security”, of the International Lith and Shota Rustaveli National Science Foundation (SRNF) (Project 216758). The Authors would like to thank the editor and two anonymous referees who kindly reviewed this manuscript and provided valuable suggestions and comments. Moreover, the Authors would especially like to thank Dr. Marco Mancini (CNR-IGAG) for giving several useful insights and the municipality of Gori for making borehole data available.

REFERENCES

- Adamia, Sh., N. Mumladze, N. Sadradze, E., N. Tsereteli, and O. Varazanashvili (2008). Late Cenozoic tectonics and geodynamics of Georgia (SW Caucasus), in *Georgian International Journal of Science and Technology* ISSN 1939-5825. Nova Science Publishers, vol. 1, issue 1, USA, 77-107.
- Adamia, Sh., V. Alania, A. Chabukiani, G. Chichua, O. Enukidze, and N. Sadradze (2010). Evolution of the Late Cenozoic basins of Georgia (SW Caucasus): a review, in *Geological Society London Special Publications* 340(1):239-259
- Aivazishvili, I., and V. Papalashvili. (1975). Ocherk seismicheskoi aktivnosti g. Gori. Monograph, Tbilisi, 26 p.
- Akin, M., S. Kramer and T. Topal (2013). Evaluation of Site Amplification of Erbaa, Tokat (Turkey). *Seventh International Conference on Case Histories in Geotechnical Engineering*. Paper 23. <http://scholarsmine.mst.edu/icchge/7icchge/session04/23>.
- Albarelo, D., and E. Lunedei (2010). Alternative interpretations of Horizontal to Vertical Spectral Ratios of ambient vibrations: new insights from theoretical modeling, in *Bull Earthq Eng* 8(3):519–534. doi:10.1007/s10518-009-9110-0.

Albarelo, D. (2017). Extensive application of seismic microzoning: methodological and socio-political issues in the Italian Experience, in *Boll.Geofis.Teor.Appl.*, Vol. 58, n. 4, pp. 253-264, DOI 10.4430/bgta0205

Albarelo, D., C. Cesi, V. Eulilli, F. Guerrini, E. Lunedei, E. Paolucci, D. Pileggi, and L. M. Puzzilli (2011). The contribution of the ambient vibration prospecting in seismic microzoning: an example from the area damaged by the 26th April 2009 l'Aquila (Italy) earthquake, in *Boll.Geofis.Teor.Appl.*, 52, 3, 513-538, DOI 10.4430/bgta0013

Albarelo, D., V.L. Socco, M. Picozzi, and S. Foti (2015). Seismic Hazard and land management policies in Italy: the role of seismic investigations, in *First Break*, 33, 87-93

Amanti, M., V. Chiessi, C. Muraro, L. M. Puzzilli, M. Roma, S. Catalano, G. Romagnoli, G. Tortorici, G. Cavuoto, D. Albarelo, et al. (2020a). Geological and geotechnical models definition for 3rd level seismic microzonation studies in Central Italy, in *Bull.Earthq.Eng.*, 18:5441–5473, <https://doi.org/10.1007/s10518-020-00843-x>

Amanti, M., L. M. Puzzilli, V. Chiessi, M. Roma, M. D'Orefice, D. Fiorenza, A. Troccoli, and F. Ferri (2020b). The seismic microzonation study of Pescara del Tronto (Central Italy) during and after the Central Italy earthquake sequence, in *Bull. Earthq. Eng.*, 18:5677–5712 <https://doi.org/10.1007/s10518-020-00927-8>

Anderson, J. G. (2007). Physical processes that control strong ground motion. In: *Treatise on geophysics*, earthquake seismology, vol 5. Schubert G (ed), Elsevier, Amsterdam, pp 513–565.

ASTM Committee D-18 on Soil and Rock (2017) Standard practice for classification of soils for engineering purposes (unified soil classification system) 1. ASTM International

Bard, P.-Y., and M. Bouchon (1980). The seismic response of sediment-filled valleys. Part 1. The case of incident SH waves, in *Bull. Seismol. Soc. Am.*, vol. 70, no. 4, pp. 1263-1286.

Bard, P.-Y., and M. Bouchon (1985). The two-dimensional resonance of sediment-filled valleys, in *Bull. Seismol. Soc. Am.*; 75 (2): 519–541.

Bard, P.Y. (1998). Microtremor measurement: a tool for site effects estimation?, *Second international symposium on the effects of the surface geology on seismic motion ESG98*, Japan.

626 Bonnefoy-Claudet, S., C. Cornou, P.-Y. Bard, F. Cotton, P. Moczo, J. Kristek, and D. Fäh (2006). H/V
 627 ratios: a tool for site effects evaluation. Results from 1-D noise simulations, in *Geophys. J. Int.*, 167, 827–
 628 837.

629 Bragato, P.L., G. Laurenzano & C. Barnaba (2007). Automatic zonation of urban areas based on the
 630 similarity of H/V spectral ratios, in *Bull. seism. Soc. Am.*, 97(5), 1404–1412, doi: 10.1785/0120060245.

631 Bramerini, F., G. Carbone, S. Castenetto, M. Coltella, G. Naso, and A. Pietrosante (2018) Commissione
 632 tecnica per la microzonazione sismica, 2017 (articolo 5, comma 7, OPCM 13 novembre 2010, n. 3907).
 633 Standard di rappresentazione ed archiviazione informatica – Versione 4.1”, Dipartimento della Protezione
 634 Civile, pp. 1-134. Available from: [https://www.centromicrozonazioneisismica.it/it/download/category/26-](https://www.centromicrozonazioneisismica.it/it/download/category/26-standardms-41)
 635 [standardms-41](https://www.centromicrozonazioneisismica.it/it/download/category/26-standardms-41)

636 Caielli, G., R. De Franco, V. Di Fiore, D. Albarello, S. Catalano, F. Pergalani, G. Cavuoto, M. Cercato, M.
 637 Compagnoni, J. Facciorusso, D. Famiani, F. Ferri, S. Imposa, G. Martini, A. Paciello, E. Paolucci, F. Passeri,
 638 S. Piscitelli, L. M. Puzzilli, and M. Vassallo (2020). Extensive surface geophysical prospecting for seismic
 639 microzonation, in *Bull. Earthq. Eng.*, 18:5475–5502, <https://doi.org/10.1007/s10518-020-00866-4>.

640 Crespellani, T., and G. Simoni (2007). Dynamic shear stiffness and damping measurements for seismic
 641 response analyses at Senigallia , Italy Détermination expérimentale des paramètres dynamiques pour l ‘
 642 analyse de la réponse du sol aux tremblements de terre a Senigallia, in: *Proceedings of the ERTC-12 Special*
 643 *Session of XIV European Conference on Soil Mechanics and Geotechnical Engineering*, ECSMGE, Madrid;
 644 2007.

645 Davis, J. C. (2002). Statistics and Data Analysis in Geology, 3rd edn, John Wiley & Sons, 656 pp. (13)
 646 (PDF) Key issues in Seismic Microzonation studies: Lessons from recent experiences in Italy. Available
 647 from:
 648 https://www.researchgate.net/publication/308793056_Key_issues_in_Seismic_Microzonation_studies_Lessons_from_recent_experiences_in_Italy
 649 [ns_from_recent_experiences_in_Italy](https://www.researchgate.net/publication/308793056_Key_issues_in_Seismic_Microzonation_studies_Lessons_from_recent_experiences_in_Italy)

650 Dolce, M., D. Albarello, S. Castellaro, S. Castenetto, A. Colombi, M. Compagnoni, M. Di Filippo, Di Nezza
 651 M., C. Eva, S. Foti et al. (2011). Contributi per l’aggiornamento degli “Indirizzi e criteri per la

652 microzonazione sismica”, *Ingegneria sismica* (Supplemento alla rivista trimestrale), 28, 2, Patron editore
653 Bologna, Italy. Available from: [https://www.centromicrozonazione-sismica.it/it/download/category/17-](https://www.centromicrozonazione-sismica.it/it/download/category/17-contributi-per-l-aggiornamento-degli-indirizzi-e-criteri-per-la-microzonazione-sismica)
654 [contributi-per-l-aggiornamento-degli-indirizzi-e-criteri-per-la-microzonazione-sismica](https://www.centromicrozonazione-sismica.it/it/download/category/17-contributi-per-l-aggiornamento-degli-indirizzi-e-criteri-per-la-microzonazione-sismica)

655 DRM - WORLD INSTITUTE FOR DISASTER RISK MANAGEMENT, INC. (2004). Seismic
656 microzonation for municipalities, Manual. Republic of Turkey, Ministry of Public Works and Settlement,
657 General Directorate for Disaster Affairs. Available from:
658 <http://www.koeri.boun.edu.tr/depremmuh/eski/MERM%20Manual.pdf>.

659 Earthquake Catalogue of Georgia (2018). Tbilisi, Georgia, Nodia Institute of Geophysics. [http://www.ig-](http://www.ig-geophysics.ge/sector1-eng.html)
660 [geophysics.ge/sector1-eng.html](http://www.ig-geophysics.ge/sector1-eng.html)

661 Foti, S. (2000). Multistation methods for geotechnical characterization using surface waves, PhD
662 Dissertation, Politecnico di Torino,
663 www.soilmech.polito.it/content/download/117/592/version/1/file/SFPhddiss.pdf.

664 Foti, S., S. Parolai, D. Albarello, and M. Picozzi (2011). Application of Surface wave methods for seismic
665 site characterization, in *Surv. Geophys.*, 32, 6, 777-825, DOI 10.1007/s10712-011-9134-2.

666 Furlani, S., G. Monegato, A. Stingen, E. Rova, D. Kupradze, G. Boschian., M. Massironi, and A.
667 Bondesan (2012). Paleohydrographic evolution and its influence on human settlement in the Medjuda Basin
668 (Georgia), in *Alpine and Mediterranean Quaternary*, 25 (1), 2012, 57-66.

669 García-Jerez, A., F. Luzón, F. J. Sánchez-Sesma, E. Lunedei, D. Albarello, M. A. Santoyo, et al. (2013).
670 Diffuse elastic wavefield within a simple crustal model. Some consequences for low and high frequencies, *J*
671 *Geophys Res Solid Earth* 2013;118:5577–5595.

672 García-Jerez, A., J. Piña-Flores J, F. J. Sánchez-Sesma, F. Luzón, and M. A. Pertón (2016). A computer code
673 for forward calculation and inversion of the H/V spectral ratio under the diffuse field assumption, in
674 *Computers & Geosciences* 2016;97:67–78. doi:10.1016/j.cageo.2016.06.016.

675 Khain, V. E., and E. Malanovsky (1963). Structure tectonique du Caucase d'après les données modernes, In:
676 *Mem. Soc. Geol. Fr.*, Volume in Honor of Prof. Paul Fallot, T. II: 663-703.

677 Konno K., and T. Ohmachi (1998). Ground-motion characteristics estimated from spectral ratio between
678 horizontal and vertical components of microtremors, in *Bull. Seismol. Soc. Am.*, 88, 228-241.

679 Kramer, S. L. (1996). Geotechnical earthquake engineering, in *Prentice Hall*, New York, 653 pp.

680 Lunedei, E., and P. Malischewsky (2015). A review and some new issues on the theory of the H/V technique
681 for ambient vibrations. A. Ansal (ed.), *Perspectives on European Earthquake Engineering and Seismology*,
682 *Geotechnical, Geological and Earthquake Engineering* 39, DOI 10.1007/978-3-319-16964-4_15.

683 Medvedev, S. V. (1965). Engineering seismology, Israel Program for Scientific Translations, available from
684 U. S. Dept. of Commerce, Clearinghouse for Federal Scientific and Technical Information, Springfield, Va.,
685 cat.1382, 260 pp.

686 Miall, A. D. (1982). Analysis of Fluvial Depositional Systems, American Association of Petroleum
687 Geologists, 75 pgs.

688 Molnar, S., J. F. Cassidy, S. Castellaro, C. Cornou, H. Crow, J. A. Hunter, S. Matsushima, F. J.
689 Sánchez-Sesma and A. Yong (2018). Application of Microtremor Horizontal-to-Vertical Spectral Ratio
690 (MHVSR) Analysis for Site Characterization: State of the Art. In *Surv Geophys* 39:613–
691 631 <https://doi.org/10.1007/s10712-018-9464-4>.

692 Moscatelli, M., D. Albarello, G. Scarascia Mugnozza, and M. Dolce (2020). The Italian approach to seismic
693 microzonation, in *Bull. Earthq. Eng.* 18:5425–5440, <https://doi.org/10.1007/s10518-020-00856-6>.

694 NEHRP (National Earthquake Hazards Reduction Program); 2004: NEHRP recommended provisions for
695 seismic regulations for new buildings and other structures (Fema 450). Building Seismic Safety Council,
696 National Institute of Building Sciences, Washington, DC, USA, 338 pp.

697 Pagliaroli, A., F. Pergalani, A. Ciancimino, A. Chiaradonna, M. Compagnoni, F. de Silva, S. Foti, S. Giallini,
698 Lanzo G, Lombardi F, et al. (2019). Site response analyses for complex geological and morphological
699 conditions: relevant case-histories from 3rd level seismic microzonation in Central Italy, in *Bull Earthq Eng.*
700 Special Issue on “Seismic Microzonation of Central Italy following the 2016–2017 Seismic Sequence”. First

Online: 15th April 2019. <https://doi.org/10.1007/s10518-019-00610-7> and morphological conditions: relevant case-histories from 3rd level seismic microzonation in Central Italy

Paolucci, E., E. Lunedei, and D. Albarello (2017). Application of the Principal Component Analysis (PCA) to HVSR data aimed at the seismic characterization of earthquake prone areas, in *Geophys. J. Int.* 211, 650–662, doi: 10.1093/gji/ggx325

Paolucci, E., A. Tanzini, G. Peruzzi, D. Albarello, and P. Tiberi (2020). Empirical testing of a simplified approach for the estimation of 1D lithostratigraphical amplification factor, in *Bull. Earthq. Eng.*, 18:1285–1301, doi: 10.1007/s10518-019-00772-4

Paolucci, R. (2002). Amplification of earthquake ground motion by steep topographic irregularities, in *Earthquake Engineering and Structural Dynamics* 31, 1831–1853.

Park, C., R. D. Miller, J. Xia (1999). Multichannel analysis of surface waves (MASW), in *Geophysics* 64(3) doi: 10.1190/1.1444590.

Peruzzi, G., D. Albarello, M. Baglione, V. D’Intinosante, P. Fabbroni and D. Pileggi (2016). Assessing 1D seismic response in microzoning studies in Italy, in *Bull. Earthq. Eng.*, 14, 373–389, doi: 10.1007/s10518-015-9841-z.

Picozzi, M., and D. Albarello (2007). Combining Genetic and Linearized algorithms for a two-step joint inversion of Rayleigh wave dispersion and H/V spectral ratio curves, in *Geophys J Int* 169:189–200.

Piña-Flores J., M. Perton, A. García-Jerez, E. Carmona, F. Luzón, J. C. Molina-Villegas, and F.J. Sánchez-Sesma (2017). The inversion of spectral ratio H/V in a layered system using the diffuse field assumption (DFA), in *Geophys J Int* 2017;208:577–88. doi:10.1093/gji/ggw416.

Reilinger, R., S. McClusky, P. Vernant, S. Lawrence, S. Ergintav, R. Cakmak, H. Ozener, F. Kadirov, I. Guliev, R. Stepanyan et al. (2006). GPS constraints on continental deformation in the Africa-Arabia-Eurasia continental collision zone and implications for the dynamics of plate interactions, in *J. Geophys. Res.*, 111(B05411), doi: 10.1029/2005JB004051.

725 Sánchez-Sesma, F. J., M. Rodríguez, U. Iturrarán-Viveros, F. Luzón, M. Campillo, L. Margerin, A. García-
 726 Jerez, M. Suarez, M. A. Santoyo and A. Rodríguez-Castellano. (2011). A theory for microtremor H/V
 727 spectral ratio: application for a layered medium, in *Geophys J Int* 2011;186:221–5. doi:10.1111/j.1365-
 728 246X.2011.05064.

729 Stinghen, A. (2011). Evoluzione tettonica e geomorfologica del Bacino di Kartalini, Georgia. Tesi di laurea
 730 specialistica in geologia, Università Degli Studi Di Padova, 109 pgs.

731 Strollo, A., S. Parolai, D. Bindi, L. Chiauzzi, R. Pagliuca, M. Mucciarelli and J. Zschau (2012).
 732 Microzonation of Potenza (Southern Italy) in terms of spectral intensity ratio using joint analysis of
 733 earthquakes and ambient noise, in *Bull. Earthq. Eng.*, 10, 2, 493-516, doi: 10.1007/s10518-011-9256-4.

734 TC4 (Technical Committee for Earthquake Geotechnical Engineering) (1999). Manual for Zonation on
 735 Seismic Geotechnical Hazard, Revised edition, Technical Committee for Earthquake Geotechnical
 736 Engineering (TC4) of the International Society of Soil Mechanics and Geotechnical Engineering (ISSMGE),
 737 209 pp.

738 Tibaldi, A., P. Oppizzi, J. Gierke, T. Oommen, N. Tsereteli, D. Odilavadze (2018). Landsliding near Enguri
 739 dam (Caucasus, Georgia) and possible seismotectonic effects, in *Nat. Hazards Earth Syst. Sci. Discuss.*,
 740 <https://doi.org/10.5194/nhess-2018-186>

741 Tsereteli, N., M. Moscatelli, D. Albarello, I. Gaudiosi, S. Giallini, Z. Gogoladze, F. Polpetta, M. Simionato,
 742 F. Stigliano, D. Svanadze, L. Danciu, O. Varazanashvili, and G. Gaprindashvili (2021). Building knowledge
 743 for geohazard assessment and management in the Caucasus and other orogenic regions. Edited on the
 744 Springer Journal: *NATO Science for Peace and Security Series*.

745 Ullah, S., D. Bindi, M. Pittore, M. Pilz, S. Parolai (2013). Improving the spatial resolution of ground motion
 746 variability using earthquake and seismic noise data: the example of Bishkek (Kyrgyzstan), in *Bull Earthq.*
 747 *Eng.*, 11, 385–399, <https://doi.org/10.1007/s10518-012-9401-8>.

748 Varazanashvili, O., N. Tsereteli, B. Sumbadze, T. and Muchadze (2006). Seismotectonic conditions and
 749 Seismic Risk in Gori, in *Bull. Georgian National Acad. Sci.*, vol. 174(3), 423-426

750 Varazanashvili, O., N. Tsereteli, and E. Tsereteli (2011). Historical earthquakes in Georgia (up to 1900):
751 source analysis and catalogue compilation, Monograph, Pub Hause MVP, Tbilisi, p. 81.

752 Varazanashvili, O., N. Tsereteli, F. L. Bonali, V. Arabidze, E. Russo, F. Pasquaré Mariotto, Z. Gogoladze, A.
753 Tibaldi, N. Kvavadze & P. Oppizziet al. (2018). GeoInt: the first macroseismic intensity database for the
754 Republic of Georgia, in *J Seismol*, 22(3), 625-667.

755 WGSM (Working Group on Seismic Microzoning) (2008). Indirizzi e criteri per la microzonazione sismica.
756 Conferenza delle Regioni e delle Province autonome – Dipartimento della Protezione Civile, Roma, 3 vol. e
757 DVD, (in Italian) available online at the website
758 http://www.protezionecivile.gov.it/jcms/it/view_pub.wp?contentId=PUB1137, English version at
759 http://www.protezionecivile.gov.it/httpdocs/cms/attach_extra/GuidelinesForSeismicMicrozonation.pdf?.

760 WGSMLA (Working Group on Seismic Microzoning the L'Aquila Area) (2010). Microzonazione sismica
761 per la ricostruzione dell'area aquilana. Regione Abruzzo, Dipartimento della Protezione Civile, 3 vols and
762 dvd, 796 pp. (in Italian), available online at the website
763 http://www.protezionecivile.gov.it/jcms/it/view_pub.wp?contentId=PUB25330.

764 Wheeler, H. E., and V. S. Mallory (1956). Factors in lithostratigraphy, in *AAPG Bulletin*, 40,2711–2723

765 Wilks, D. S. (2006). Statistical Methods in the Atmospheric Sciences, 2nd edn, Academic Press, p. 630.

766 Zare, M., H. Amini, P. Yazdi, K. Sesetyan, M. B. Demircioglu, D. Kalafat, M. Erdik, D. Giardini, M. Asif
767 Khan, and N. Tsereteli et al. (2014) Recent developments of the Middle East catalogue, in *J Seismol*, 18(4),
768 749–772.

769

AUTHOR'S AFFILIATION

Giallini S.^{1*}, Paolucci E.², Sirianni P.¹, Albarello D.², Gaudiosi I.¹, Polpetta F.¹, Simionato M.¹, Stigliano F.¹, Tsereteli N.³, Gogoladze Z.³ and Moscatelli M.¹

1 Istituto di Geologia Ambientale e Geoingegneria (IGAG), Consiglio Nazionale delle Ricerche (CNR), Area della Ricerca di Roma 1, Montelibretti, Italy

2 Dipartimento di Scienze Fisiche, della Terra e dell'Ambiente, Università degli Studi di Siena, Siena, Italy

3 M. Nodia Institute of Geophysics of I. Javakhishvili Tbilisi State University, Tbilisi, Georgia

Corresponding author: Silvia Giallini (silvia.giallini@igag.cnr.it)

LIST OF FIGURE CAPTIONS

Figure 1. Flow diagram showing the sequence of steps composing the proposed procedure.

Figure 2. a) Tectonic map of the Arabia-Eurasia collision zone (modified from Tibaldi et al., 2018). Abbreviations: GC-Greater Caucasus; LC-Lesser Caucasus; ATFT-Acharya-Trialeti Fold-and-Thrust belt; R-Rioni; Dz-Dzirula; K-Mtkvari; MB-Mus Basin; EP-Eastern Pontides; KM-Kirsehir Massif; EAF-Eastern Anatolian Fault; NAF-North Anatolian Fault; IAES-Izmir-Ankara-Erzincan Suture; MM-Menderes Massif; The black inset refers to the location of Figure 2b; b) geographical location of Shida-Kartli Region. The white inset refers to the enlarged geological sketch of Figure 2c; c) Sketched geological map of the Kartli Basin (modified after Stinghen, 2011). The legend referred to in Figure 2c is reported at the bottom of the figure..

Figure 3. Scheme of active faults and seismicity of the Gori area. Active Faults: ATFT-Acharya-Trialeti Fold-and-Thrust belt; RLF-Racha-Lechkhumi; TF-Tkibuli; IF-Ilto; ALF-Alazani; OF-Orkhevi; EF-Eldari; KF-Kaspi; SF-Surami; AF-Atskuri; BF-Bakuriani; TWF-Tabatskuri W; TEF-Tabatskuri E; ABF-Abuli; JF-Javakheti; DF-Dmanisi; TELF-Teleti; QF-Qeda. Seismogenic zones (SSZs) lying in the study area are represented using different shades of gray, directly proportional to the maximum earthquake magnitude (M_{max}). Black circles refer to historical earthquakes, while light grey circles refer to the instrumental ones

Figure 4. Investigation map for the study area with the locations of already available data (borehole investigations) and newly performed surveys (HVSr and MASW tests). Coordinate system: WGS 1984 – UTM Zone 38N.

Figure 5. Principal Components of the HVSr data in the Gori urban area “dominating” at least one site where HVSr values have been measured. Solid and dashed curves, respectively, represent “characteristic” HVSr curves with positive and negative “polarities” depending on the sign of the corresponding “loading”. The “scores” values, located in the ordinate axis, represent the elements of the rows of the matrix (see the text for details).

Figure 6. The symbols in the map represent the locations of the single-station HVSr measurements, and their types and colors (black or white) indicate the relevant “dominant” PC. The dashed black lines in the map represent the preliminary zonation performed following the spatial distribution of the dominant PCs. Each of the 7 detected zones is marked by an identification number. The insets show the experimental (black thin lines) and the mean (black thick lines) HVSr curves for each detected zone. Black arrows in the insets highlight the resonance frequency values identified by the mean HVSr curves.

Figure 7. EG_map of Gori (a) and related cross sections (b, c), The meaning of the codes used are described within the legend and also reported in Table 3 (eg_units). The map also presents a synthesis of available data (borehole logs; geophysical investigations; PCA zonation and geological detected domains).

Figure 8. Seismically Homogeneous Microzones Map of Gori reporting the linear features of the identified buried morphology, positions of boreholes, and geophysical tests (HVSr and MASW); b) Reference logs illustrating the type-stratigraphy of Microzones 1–9.

TABLES

Table 1. Information related to historical and instrumental earthquakes that struck the Gori area. Epicentral location is reported in Figure 2

Year	M _w	I ₀ (MSK)	Record
1275	6.5	IX	Historical*
1805	4.8	V-VI	Historical*
1868	4.5	IV-V	Historical*

1878	4.7	V-VI	Historical*
1881	4.5	V	Historical*
1890	5.6	VII	Historical*
1891	4.9	V-VI	Historical*
1894	5.2	VI	Historical*
1899	6.1	IX-X	Historical*
1912	4.8	V-VI	Instrumental
1920	6.2	IX	Instrumental
1929	4.8	V-VI	Instrumental
1934	4.8	V	Instrumental
1940	6.1	VIII	Instrumental
1951	4.9	VI	Instrumental
1991	6.9	IX	Instrumental
1994	4.7	V	Instrumental

*From Varazanashvili et al., 2011; Varazanashvili et al., 2018; Earthquake Catalog of Georgia, 2018; Zare et al., 2014

Table 2. Vs profiles from joint inversions of Rayleigh wave velocity and HVSr curves (for locations, see Figure 3). Light grey band highlights the resonance interface

Depth (m)	Thickness (m)	Vs (m/s)	Depth (m)	Thickness (m)	Vs (m/s)
MW1			MW4		
2.5	2.5	315	4.15	4.15	245
9.5	7	500	9.45	5.3	575
14	4.5	665	15.85	6.4	600
21.3	7.3	955	20.45	4.6	605
30	8.7	1025	30	9.55	895
MW2			MW5		
1	1	305	1.25	1.25	100
8.3	7.3	310	2.25	1	215
12.3	4	375	7.05	4.8	270
24.6	12.3	425	11.05	4	586
30	5.4	700	13.05	2	590
			30	16.95	905
MW3			MW6		
4.4	4.4	265	3.1	3.1	180
6.2	1.8	295	7.5	4.4	505
11.65	5.45	325	9.1	1.6	570
16.35	4.7	345	16.5	7.4	920
26.75	10.4	675	30	13.5	1030
30	3.25	750			

Table 3. Correlation between lithostratigraphic units (gg_units) of the covering terrains and geological bedrock formation occurring in the studied area and engineering-geological units (eg_units)

	gg_units	gg_units_description	depositional ambient	eg_units
--	----------	----------------------	----------------------	----------

COVERING TERRAINS	Holocene alluvial deposits	Silty gravels with presence of thiny loamy/clayey layers	Banks/bars/canals	GM-es
	Holocene alluvial deposits	Sandy clays/silty clays	Banks/bars/canals	CL-es
	Holocene alluvial deposits	Gravelly sands	Banks/bars/canals	SW-es
	Pleistocene terraced deposits	Gravels and conglomerates	Fluvial terrace	GW-tf
GEOLOGICAL BEDROCK	Oligocene deposits	Highly fractured/weathered alternation of stratified sandstone to marls lithofacies, with conglomerates	Terrigenous/shallow marine	SFGRS
	Oligocene deposits	Alternation of stratified sandstone to marls lithofacies, with conglomerates	Terrigenous/shallow marine	GRS
	Eocene deposits	Highly fractured/weathered alternation of stratified sandstone to mudstone lithofacies	Turbiditic environment	SFALS
	Eocene deposits	Alternation of stratified sandstone to mudstone lithofacies	Turbiditic environment	ALS

FIGURES

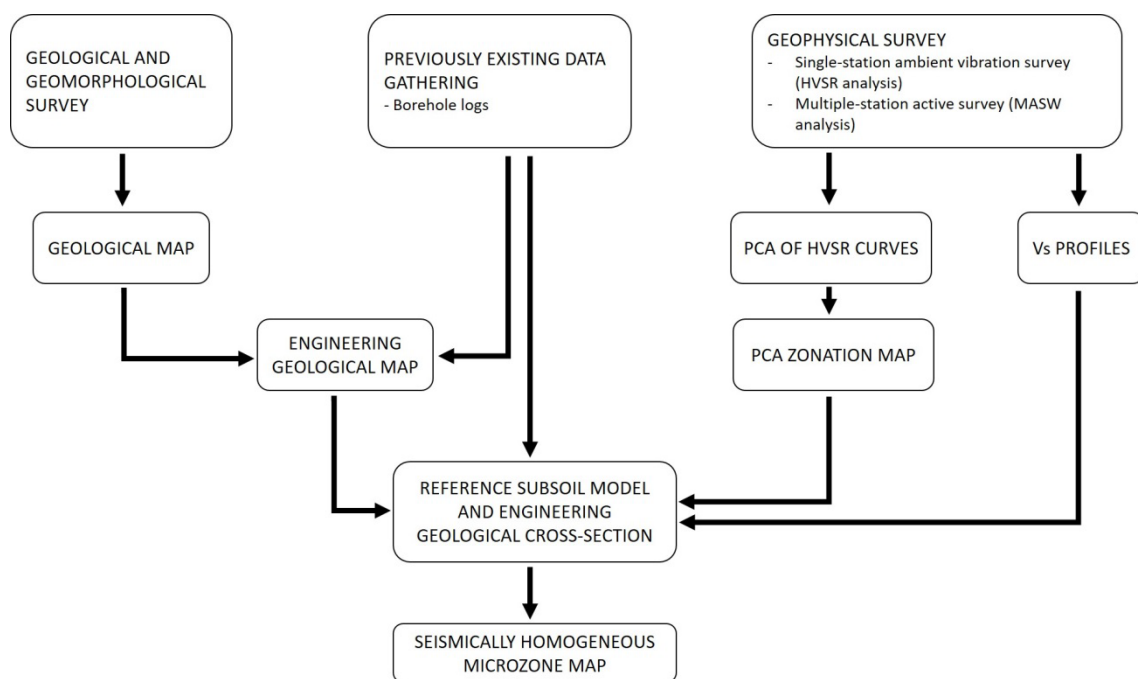


Figure 1. Flow diagram showing the sequence of steps composing the proposed procedure.

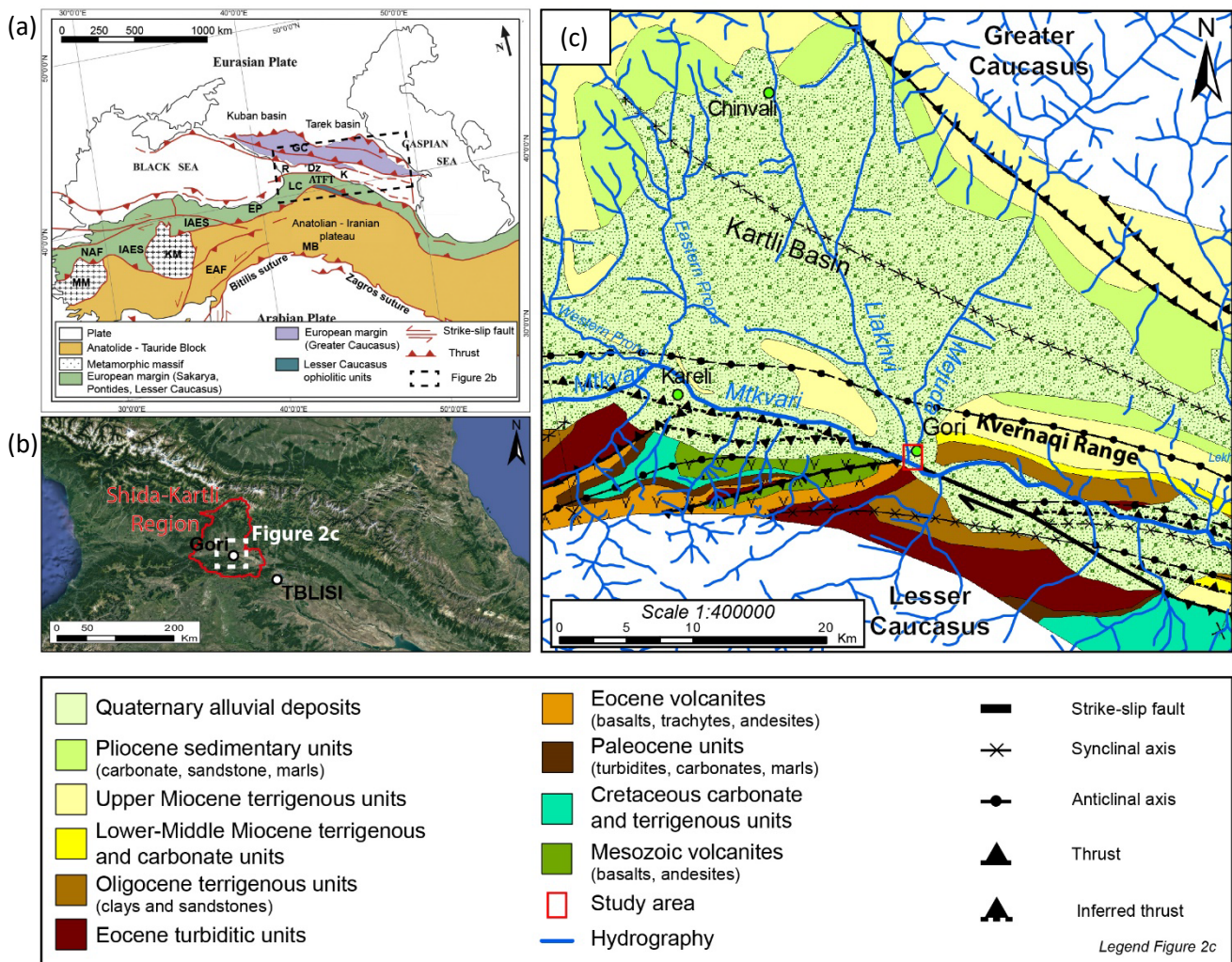


Figure 2. a) Tectonic map of the Arabia-Eurasia collision zone (modified from Tibaldi et al., 2018). Abbreviations: GC-Greater Caucasus; LC-Lesser Caucasus; ATFT-Achara-Trialeti Fold-and-Thrust belt; R-Rioni; Dz-Dzirula; K-Mtkvari; MB-Mus Basin; EP-Eastern Pontides; KM-Kirsehir Massif; EAF-Eastern Anatolian Fault; NAF-North Anatolian Fault; IAES-Izmir-Ankara-Erzincan Suture; MM-Menderes Massif; The black inset refers to the location of Figure 2b; b) geographical location of Shida-Kartli Region. The white inset refers to the enlarged geological sketch of Figure 2c; c) Sketched geological map of the Kartli Basin (modified after Stinghen, 2011). The legend referred to in Figure 2c is reported at the bottom of the figure.

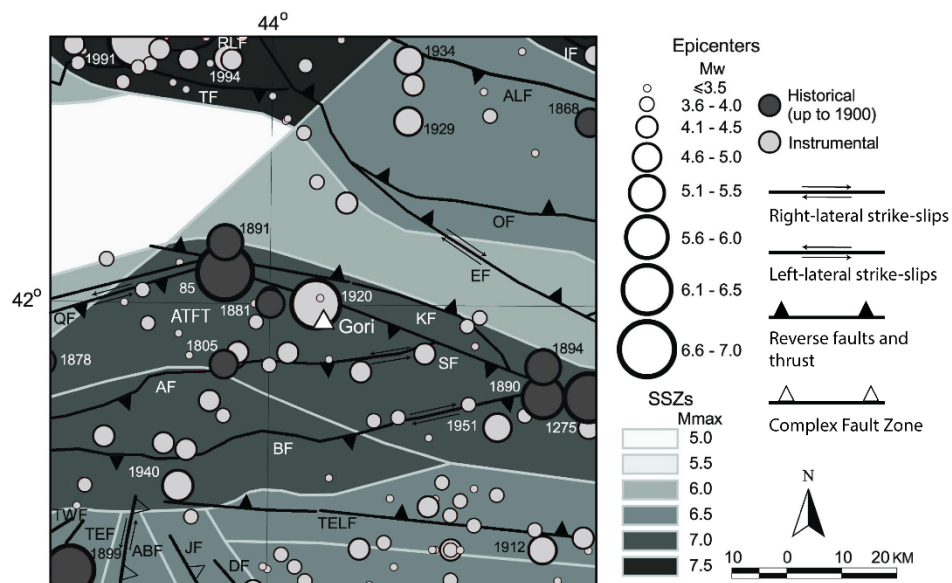


Figure 3. Scheme of active faults and seismicity of the Gori area. Active Faults: ATFT-Achara-Trialeti Fold-and- Thrust belt; RLF-Racha-Lechkhumi; TF-Tkibuli; IF-Ilto; ALF-Alazani; OF-Orkevi; EF-Eldari; KF-Kaspi; SF-Surami; AF-Atskuri; BF-Bakuriani; TWF-Tabatskuri W; TEF-Tabatskuri E; ABF-Abuli; JF-Javakheti; DF-Dmanisi; TELF-Teleti; QF-Qeda. Seismogenic zones (SSZs) lying in the study area are represented using different shades of gray, directly proportional to the maximum earthquake magnitude (Mmax). Black circles refer to historical earthquakes, while light grey circles refer to the instrumental ones.

835

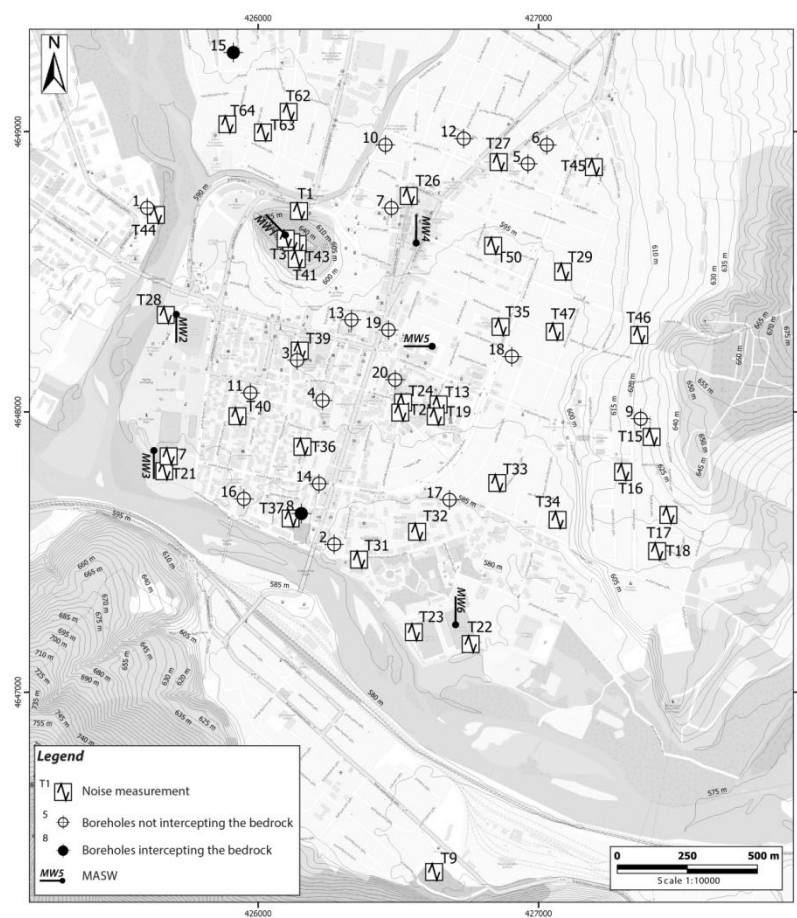


Figure 4. Investigation map for the study area with the locations of already available data (borehole

investigations) and newly performed surveys (HVSr and MASW tests). Coordinate system: WGS 1984 – UTM Zone 38N.

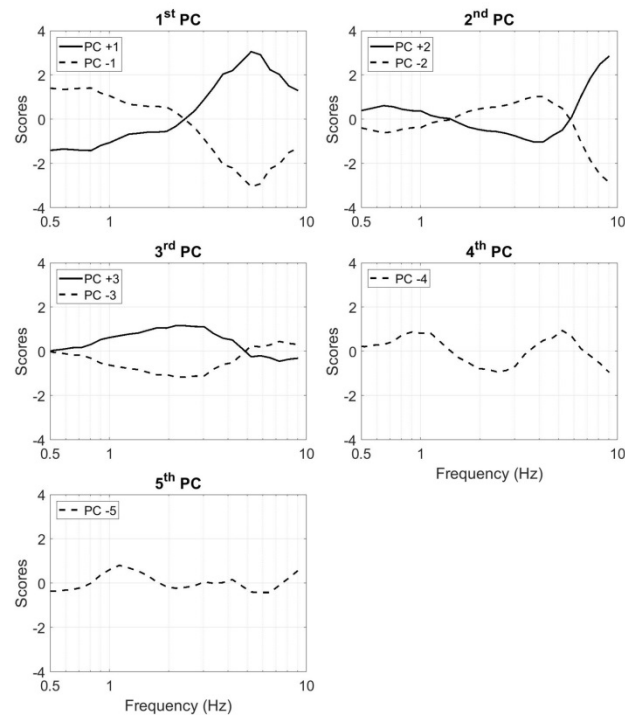


Figure 5. Principal Components of the HVSr data in the Gori urban area “dominating” at least one site where HVSr values have been measured. Solid and dashed curves, respectively, represent “characteristic” HVSr curves with positive and negative “polarities” depending on the sign of the corresponding “loading”. The “scores” values, located in the ordinate axis, represent the elements of the rows of the matrix (see the text for details).

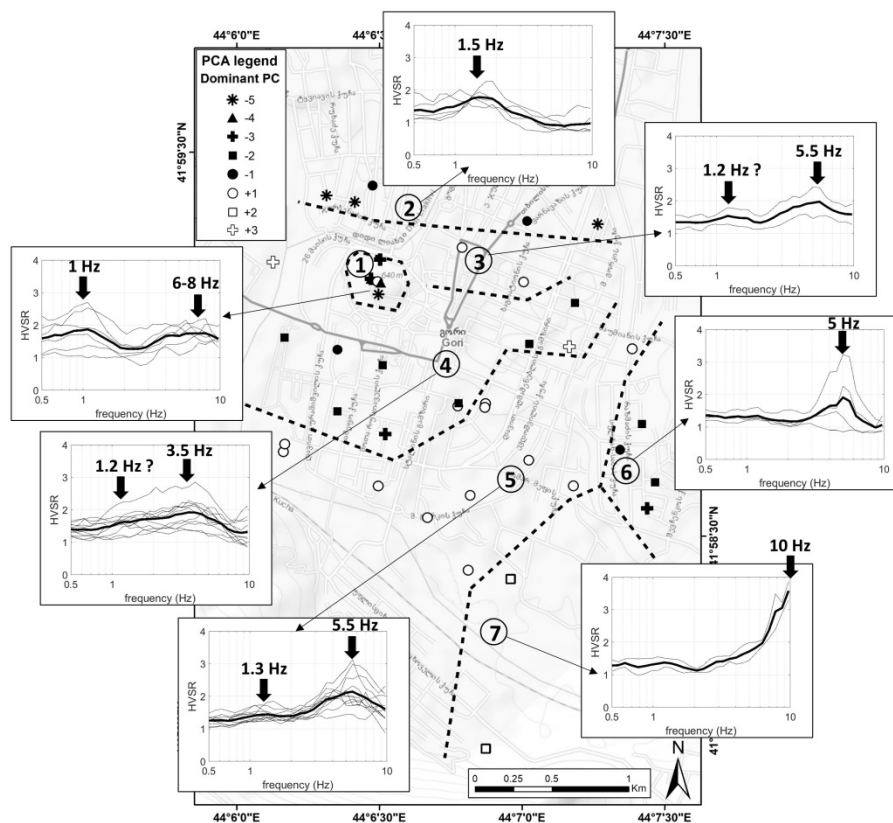


Figure 6. The symbols in the map represent the locations of the single-station HVSR measurements, and their types and colors (black or white) indicate the relevant “dominant” PC. The dashed black lines in the map represent the preliminary zonation performed following the spatial distribution of the dominant PCs. Each of the 7 detected zones is marked by an identification number. The insets show the experimental (black thin lines) and the mean (black thick lines) HVSR curves for each detected zone. Black arrows in the insets highlight the resonance frequency values identified by the mean HVSR curves.

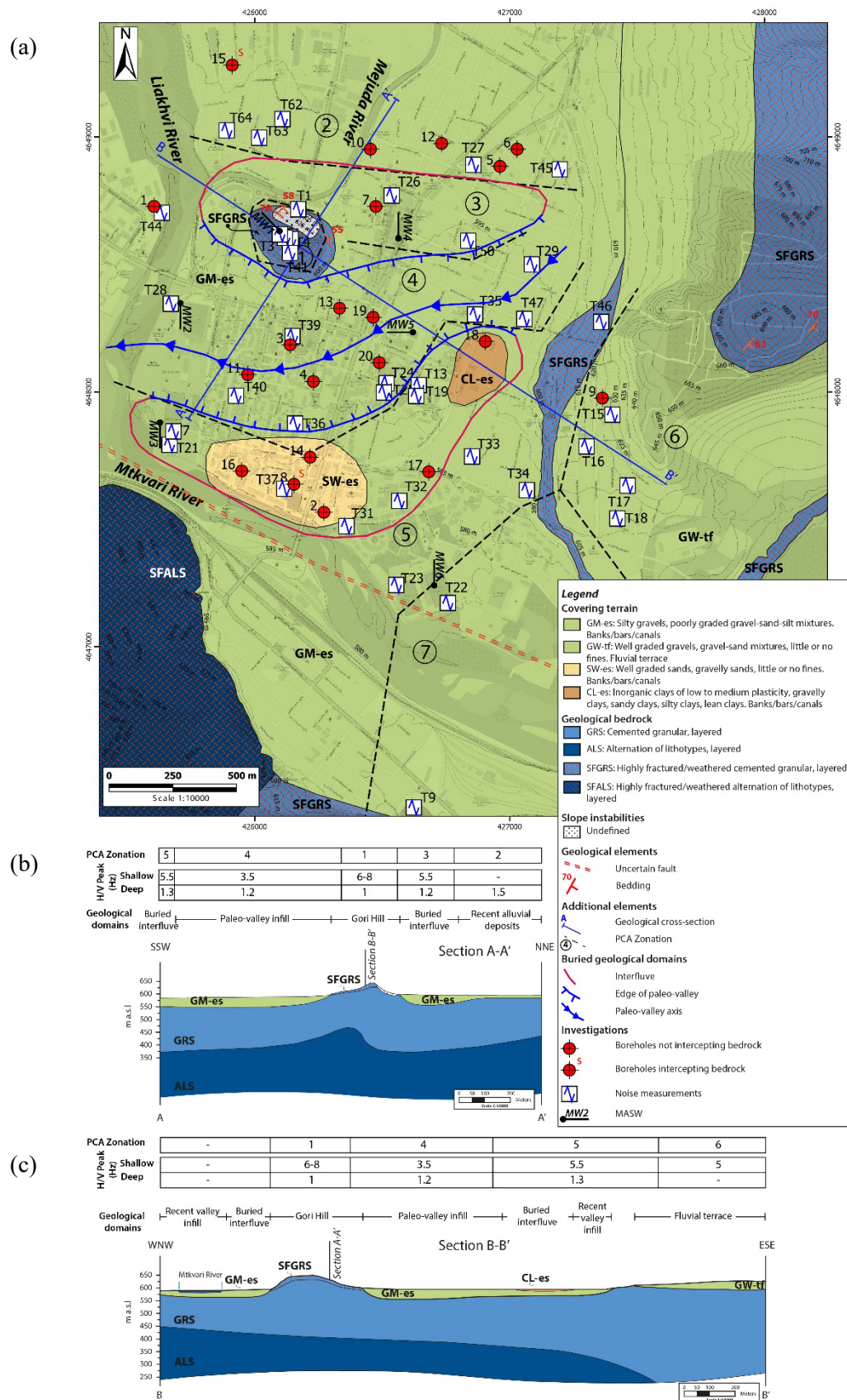


Figure 7. EG_map of Gori (a) and related cross sections (b, c), The meaning of the codes used are described within the legend and also reported in Table 3 (eg_units). The map also presents a synthesis of available data (borehole logs; geophysical investigations; PCA zonation and geological detected domains).

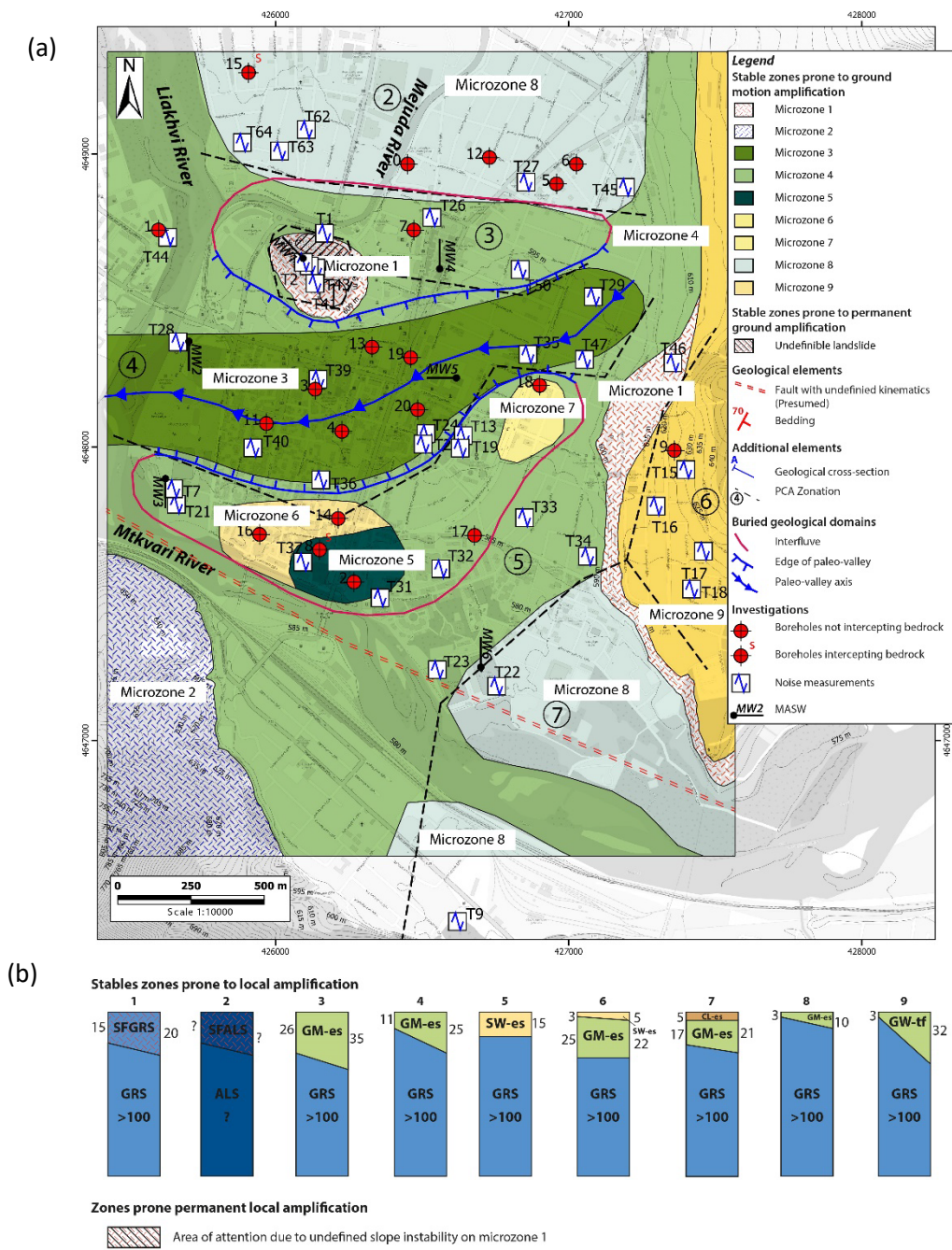


Figure 8. a) Seismically Homogeneous Microzones Map of Gori reporting the linear features of the identified buried morphology, positions of boreholes, and geophysical tests (HVSr and MASW); b) Reference logs illustrating the type-stratigraphy of Microzones 1–9.